The dendrite growth in 3D structured lithium metal anodes: Electron or ion transfer limitation?

Rui Zhang, Xin Shen, Xin-Bing Cheng, Qiang Zhang [*]

Beijing Key Laboratory of Green Chemical Reaction Engineering and Technology, Department of Chemical Engineering, Tsinghua University, Beijing 100084, China

ABSTRACT

Lithium metal is among the most promising anode materials in next-generation energy-storage systems. However, the practical applications of lithium metal batteries have been severely hindered by the uncontrollable growth of lithium dendrites. If the mechanisms behind the lithium dendrite growth behavior are well understood and the critical condition to determine the rate limitation in electroplating and stripping process are clarified, it is feasible to boost the stable cycling of composite anode through the rational design of 3D structured lithium metal anodes. Herein we employed phase field model to quantitatively describe the lithium dendrite growth in various conductive structured lithium anodes. We found that the structural areal surface area linearly determines the electroplating reaction rate in the forepart kinetic process, which is limited by electron transfer in the composite Li metal anode. Meanwhile, the structural pore-volumetric surface area exhibits an inversely proportional relationship on the electroplating reaction rate in later kinetic process, which is limited by ion transfer in electrolyte. Structured lithium metal anodes with larger areal surface area and smaller pore-volumetric surface area can be much better for high rate and high capacity battery cycling.

1. Introduction

Lithium (Li) metal is the most promising anode materials in the next-generation energy-storage systems owing to its ultrahigh theoretical specific capacity (3860 mAh g^{-1}) and the lowest negative electrochemical potential (−3.040 V *versus* standard hydrogen electrode). However, the practical applications of lithium metal anodes in lithium metal batteries (such as lithium–sulfur (Li–S), lithium–oxygen (Li–O$_2$) batteries, and other solid state batteries with Li metal anodes) have been severely hindered by uncontrollable lithium electroplated morphology [1–3]. Lithium dendrites are easily produced due to the intrinsic lattice and surface energy properties of lithium during the electroplating process of metal anodes. Since the dendritic morphology is always accompanied by a large specific surface area, the appearance of lithium dendrites tends to form more solid electrolyte interphase (SEI) layers due to the parasitic reactions between fresh lithium and electrolyte [4,5]. Besides, lithium dendrites are easily broken during their dissolution process and then detached from the current collectors in the electrostripping process. The "dead lithium" is therefore achieved and also brings irreversible capacity loss. Furthermore, the unstable SEI layer is easily cracked in the repeating morphology deformation and volume change, which causes increasing

lithium dendrite growth, redundant SEI layer, and "dead lithium" accumulation after charge and discharge cycles [6,7]. These phenomena render lithium metal anodes easily pulverized, which further induces rechargeable batteries with serious capacity decay, shorted lifespan, and even safety hazard [8,9].

A mass of strategies have been proposed to inhibit lithium dendrite growth and stabilize SEI layer, including the electrolyte additives [10–12], modified separators/artificial protective layers [13–17], solid-state electrolytes [18–21], and also the employment of designed structured anodes [22–29]. If a practical lithium metal battery is built with a very high energy density of more than 400 Wh kg^{-1}, the areal loading of electrode is expected to be more than 6 mAh cm^{-2}, which is corresponding to plating/stripping of lithium metal anode with a thickness of more than 30 μm. Except for lithium dendrite issues, the lithium metal anodes have a theoretically infinite volume change before and after plating, especially for such an ultrathin thickness of 30 μm. To avoid the volume shrink/expansion in a working battery and render a dendrite-free deposition, 3D structured lithium metal anodes, which possess customizable conductive framework for electron transfer and designable pore structures for ion transfer, are therefore strongly considered.

In terms of electron transfer: (1) the conductive framework with a

high surface area can reduce the local current density, with which can lithium metal be plated and stripped at a mild local reaction rate to maintain a dendrite-free morphology [23,30–37]; (2) the abundant electronic reaction interfaces provided by the high conductive surface area can also reduce electron transfer impedance, leading to a decreased overpotential during charge and discharge cycles [38,39]; (3) the internally connected conductive framework can also keep the lithium metal in steady electronic contact with the current collectors during uneven lithium stripping process, preventing the formation of "dead lithium" [40]; (4) the conductive surface also plays a critical role in the lithium nucleation. With the surface modification of structured surface such as lithiophilic surface [41–48], the lithium nucleation sites can be densely and uniformly distributed.

While in terms of ion transfer: (1) the pore structure can heavily determine the ionic migration, especially when part of the pore space is occupied by plated lithium. The rapid consumption of lithium ions in structured lithium metal anode can reduce the electrochemical performance and produce lithium dendrites if the lithium ionic migration supply cannot be fully satisfied [49–51]; (2) the high surface area of structured lithium metal anodes affords a large amount of SEI layer in routine liquid electrolyte, which increases the ion transfer overpotential during repeated cycles [52]. The various electrode-electrolyte interface with SEI layer may also be involved in the fast galvanic corrosion of lithium, with which the corroded lithium may be vulnerable to dendrite growth [53].

The determination of electrochemical reaction rate in 3D structured lithium metal anodes are always changed from electron transfer to ion transfer, with a decrease in electrochemical performance and finally a possibility of losing control on electroplated lithium [54,55]. However, it is incapable of giving the critical charge-discharge conditions which make the change in electrochemical reaction rate limitation, especially for a variety of 3D structured lithium metal anodes with different components and structures. The principle on rational design of 3D porous host to boost the stable cycling of composite anode is heavily lacking due to the grand challenges of current trial-and-error investigation based on complex materials innovation. If a quantitative theoretical analysis can be proposed, reliable lithium metal anodes with 3D host are highly expected.

In this contribution, phase field model is employed to numerically describe the lithium dendrite growth in various 3D conductive structured lithium metal anodes. We proposed a novel processing method to calculate deposit surface area of lithium dendrites. Such deposit surface area allows us to capture the quantity of continuously formed SEI layer. The structural areal surface area S_A ($S_{\text{current collector total surface}}/S_{\text{electrode}}$) linearly determines the electroplating reaction rate in the forepart kinetic process, which is limited by electron transfer in the composite Li metal anode. Meanwhile, the structural pore-volumetric surface area S_V ($S_{\text{current collector total surface}}/V_{\text{pores in electrode}}$) exhibits an inversely proportional relationship on the electroplating reaction rate in later kinetic process, which is regulated by ion transfer in electrolyte.

2. Results and discussions

The structured lithium metal anodes in our two-dimension models consist of ideal electronic conductive vertical channels. This renders the fact that the electrons on the surface of structured anodes are always sufficient for rapid electrochemical reactions. The vertical channels are with a channel width (pore diameter) of d and a channel length of h (Fig. 1). The lithium nucleation sites can be achieved on structural surface with the same space interval on structured lithium metal anode at the initial electroplating process. During the subsequent electroplating of lithium metal, the lithium ions in the electrolyte near the nucleation sites begin to be rapidly consumed. The lithium ions in the bulk phase of the electrolyte are difficult to diffuse and migrate to the deposit surface in time, especially at high current rate and high charge capacity. Therefore, a lithium ion consumption region with a very low lithium ion
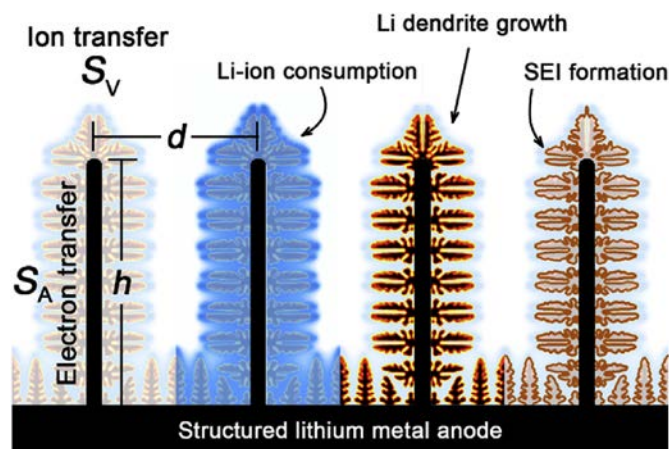

Fig. 1. Schematic illustration of the simulated structured lithium metal anode. The conductive vertical channels are with a size of $h \times d$. The consumption of lithium ions aggravates lithium dendrite growth in the process of lithium electroplating, which finally produce a high surface area with further SEI formation. The electron transfer is controlled by structural areal surface area S_A, and the ion transfer is controlled by structural pore-volumetric surface area S_V.

concentration is formed. The growth of lithium dendrites on the structural surface starts at the same time. Once the lithium dendrite grows, the total surface area of lithium-electrolyte interface on the grown lithium dendrites will also gradually increases. Since the fresh active lithium metal reacts with the electrolyte instantaneously to form SEI layer, the area of the SEI layer is also gradually increased. Therefore, the lithium dendrite growth process is accompanied by continuous irreversible consumption of the electrolyte and lithium metal anode. That in turn significantly reduces the Coulombic efficiency and cycle lifespan of working lithium metal batteries.

In order to describe the lithium dendrite growth with continuously transforming and moving solid-liquid sharp interface, phase field theory introduces an order parameter ξ to investigate diffuse interface, rather than sharp interface in traditional models [56,57]. The phase field order parameter ξ equals to 0 and 1 in the electrolyte liquid phase and the lithium metal solid phase, respectively. The value of ξ varies from 0 to 1 in the interfacial region, representing the diffuse interface with continuous physical and chemical parameters expressed as functions of ξ. The phase field model simulated herein is based on the nonlinear phase field lithium dendrite model proposed by Chen and co-workers [58]. The detailed simulation methods can be found in Experimental Section.

The lithium dendrite growth simulated by the nonlinear phase field model consists with the experimental results in growth behavior and morphology. Fig. 2a and b exhibit the simulated Li ion concentration and phase field order parameter evolution of electroplated lithium metal on plane surface with single lithium nucleation site at a plating duration at 0, 5, and 10 min. In the dendritic morphology evolution snapshots (Fig. 2b), the region with phase field order parameter $\xi = 0$ represents the liquid electrolyte phase, and that with $\xi = 1$ represents the solid lithium metal phase. Besides, the region with ξ between 0 and 1 represents the electrode electrolyte interface, whose thickness is just virtual numerical result. The lithium ions will be rapidly consumed to nearly zero concentration around the nucleation sites during the electroplating process, and at the same time tree-like lithium dendrite begins to grow.

With one single nucleation site, the lithium dendrite not only vertically grows toward the bulk electrolyte from the bottom, but also grow in the lateral direction with a comparable rate of electrodeposition. As a result, the lithium dendrite grows with a radial pattern, which exhibits a gradually enlarged external contour of an equilateral right triangle in two-dimension model (Movie S1, Supporting Information). Such radial growth pattern can be verified in the *in-situ* optical microscopic observation. The electroplated lithium grows from a single nucleation site to a
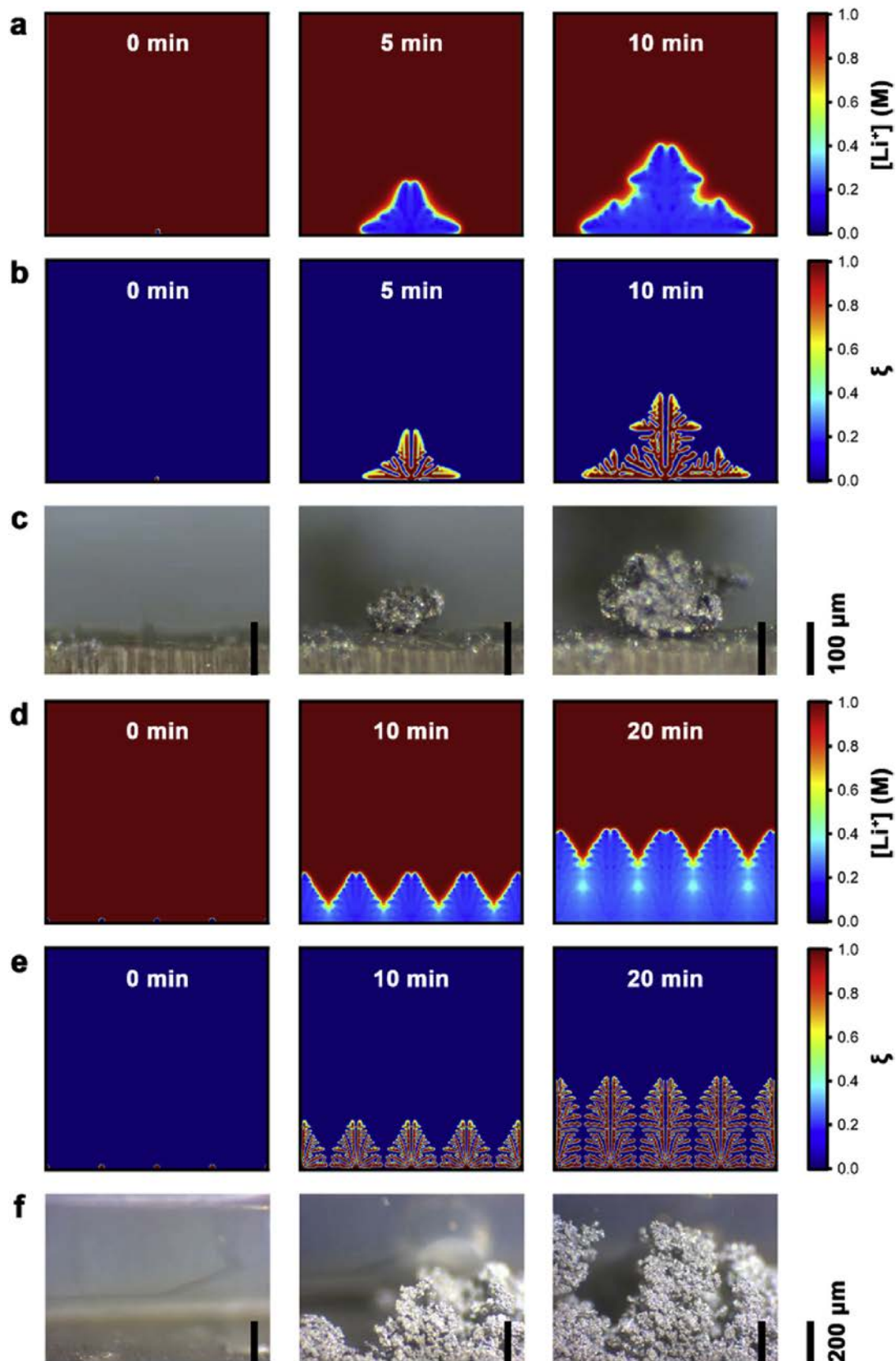
Fig. 2. The simulated and *in-situ* optical microscopic results of lithium dendrites. The simulated a,d) Li ion consumption and b,e) dendritic morphology evolution during lithium electroplating on plane surface with a,b) single and d,e) multiple lithium nucleation sites, respectively. c,f) *In-situ* optical microscopy photos of lithium dendrite growth during lithium electroplating on plane surface with c) single or f) multiple lithium nucleation sites, respectively.

large tree-like dendrite at all hemispherical directions on electrode surface (Fig. 2c, Movie S2, Supporting Information). When the lithium is electroplated on plane surface with multiple lithium nucleation sites, which with an initial nucleation interval of 50 μm, the Li ion consumption and the lithium dendrite growth during the forepart of electroplating process is the same radial growth pattern. However, when the dendrites grown by the adjacent two nucleation sites are in contact with each other at 10 min, they will change the growth behavior from radial growth to one-dimensional vertical growth perpendicular to the electrode surface, due to the space limitation and the only lithium ion supply route from the top bulk electrolyte (Fig. 2d and e). In the *in-situ* optical microscopic

experiments, the lithium dendrite growth is also experience the growth pattern changes from radial pattern to aligned array growth. After the growth contact of adjoining dendrites, they all continue to grow only at vertical direction into long dendrites (Fig. 2f, Movie S3, Supporting Information). In addition, lithium dendrites are always with various patterns in experimental results, due to the different surface roughness, various internal stress, ever-changing SEI compositions and structures, and uneven distributions of electrons and ions. In order to have comparable results with different structured lithium metal anodes, these factors are not taken into account in this work.

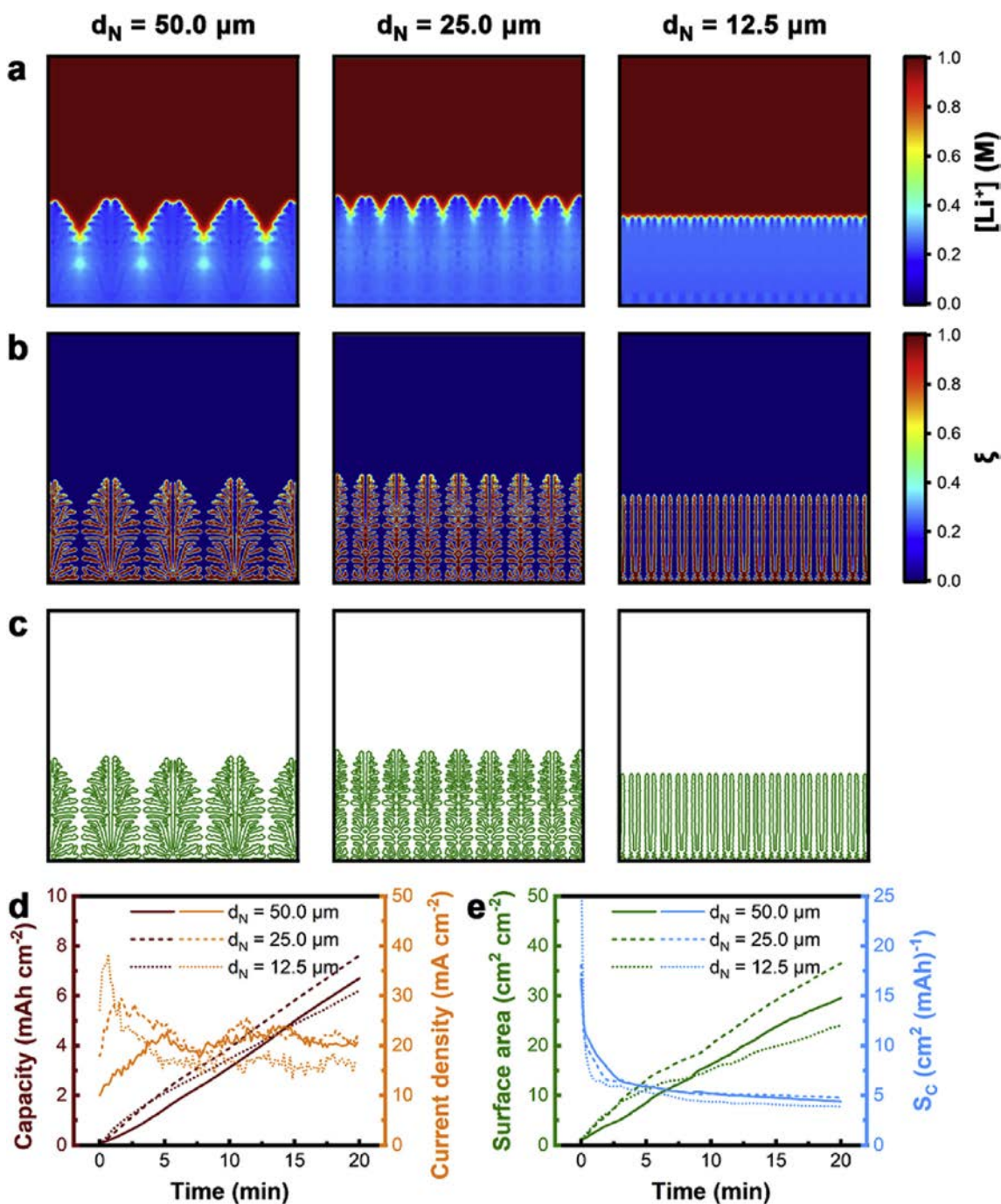Supplementary video related to this article can be found at https://do

Fig. 3. The simulated lithium dendrite morphology on plane surface with different nucleation intervals. The simulated a) Li ion concentration and b) final dendritic morphology after lithium electroplated on plane surface with different nucleation intervals ($d_N = 50.0$, 25.0, and 12.5 μm). c) The produced surface profile of lithium dendrites from b). d) The electroplated capacity and current density curves with different nucleation intervals. e) The total surface area and surface area per capacity curves with different nucleation intervals.

The lithium dendrite growth morphologies with different initial nucleation intervals have also been explored. The final Li ion concentration distributions and dendritic morphologies after 20 min electroplating on plane surface with different nucleation intervals ($d_N = 12.5$, 25.0, and 50.0 μm) exhibit the similar growth behavior with mode switching from radial growth to vertical growth (Fig. 3a and b, and Movie S4, Supporting Information). In order to have a clear dendritic profile and quantitative analysis on its shape and surface area, the lithium dendrite profile data are extracted from calculated phase field order parameters, which has never been touched in previous experiments or simulations. Since the diffuse interface where ξ is between 0 and 1 is a numerical interface with a numerical thickness, which does not correspond to the actual thickness of SEI layer. The contour line at $\xi = 0.5$ which indicates the numerical position of solid-electrolyte interface is selected as the surface profile of electroplated lithium dendrites (Fig. 3c).

Supplementary data related to this article can be found at https://doi.org/10.1016/j.ensm.2019.03.029.

When the initial lithium nucleation density is increased, the branches of lithium dendrites are shorten and even nearly disappear when the initial nucleation interval d_N is 12.5 μm. However, the trunk of every lithium dendrites are with the same length. The top surface of the Li deposits is also significantly smoother at a smaller initial nucleation interval. The roughness of the deposit surface decreases from 50 to 6 μm, while d_N reduces from 50.0 to 12.5 μm (Fig. 3c). After the 20 min

electroplating process, the electroplated areal capacities all increase almost linearly to 6.21, 7.61, and 6.70 mAh cm^{-2}, indicating a relatively stable and similar average current density of 18.6, 22.8, and 20.1 mA cm^{-2} at a set constant overpotential of 0.10 V with the different nucleation intervals of 12.5, 25.0, and 50.0 μm, respectively (Fig. 3d). However, It is worth noting that in the initial 5 min electroplating, the starting current density can reach 38.3, 29.5, and 22.6 mA cm^{-2} at a nucleation interval of 12.5, 25.0, and 50.0 μm, respectively. There is an obvious accelerate in starting electroplating reaction rate with a small nucleation interval, which is also predicting the small beginning overpotential during galvanostatic charging process reported in many previous publications (Fig. 3d) [31,43].

The deposit areal surface area with different nucleation intervals also increase almost linearly to 24.1, 36.5, and 29.6 cm^2 cm^{-2}, respectively. Besides, there is a convergent surface area per unit capacity S_c (the ratio of total deposit surface area to the plated capacity) of 3.9, 4.8, and 4.4 cm^2 (mAh)$^{-1}$ at a prolonged electroplating with different nucleation intervals of 12.5, 25.0, and 50.0 μm, respectively. This indicates that the increasing SEI layer formation is proportional to the continuous electroplating of lithium metal, but no obvious relationship with nucleation interval (Fig. 3e). Therefore, the nucleation intervals can determine the final lithium dendrite morphology. The deposits can become smoother with smaller nucleation intervals. A small nucleation interval can distinctly increase the reaction rate during potentiostatic process or decrease the overpotential during galvanostatic process. However, the
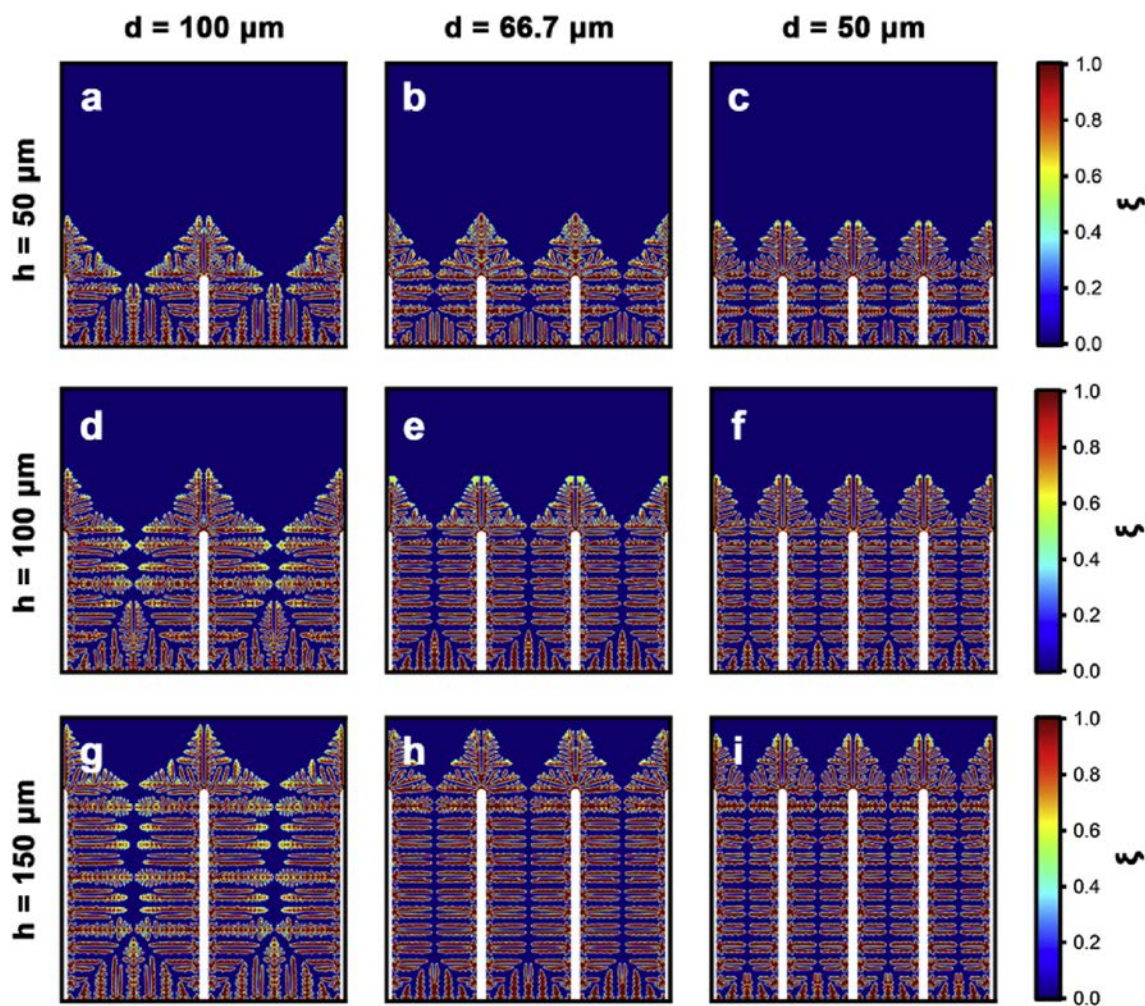

Fig. 4. The simulated lithium dendrite morphology in various structured lithium metal anodes. The simulated final dendritic morphology after lithium electroplated in structured lithium metal anodes with different channel widths (d = (a,d,g) 100, (b,e,h) 66.7, and (c,f,i) 50 μm) and different channel lengths (h = (a,b,c) 50, (d,e,f) 100, and (g,h,i) 150 μm).

nucleation intervals make little different to the average plating current density and dendritic surface area during prolonged electroplating process. Additionally, Cui and co-workers have found that the lithium nuclei size is proportional to the inverse of overpotential, and the number density of lithium nuclei is proportional to the cubic power of overpotential, which can help set up models with more precise nucleation intervals [59].

The lithium dendrite growth in various structured lithium metal anodes with different channel widths d and different channel lengths h is presented in Fig. 4, and the lithium ion concentration evolution can be found in Fig. S1, Supporting Information. The structural areal surface areas S_A (the ratio of initial structural electronic conductive surface area to the 3D electrode frontal sectional area) and the structural pore-volumetric surface areas S_V (the ratio of initial structural electronic conductive surface area to the total pore volumes in 3D electrode) of these various structured lithium metal anodes can be found in Table 1. In order to achieve comparable results, and considering the little influence induced by nucleation intervals during prolonged electroplating process discussed above, we employ a uniform initial nucleation interval of 12.5 μm in these structured lithium metal anodes.

When the channel width d decreases from 100 to 50 μm, taking the structure with the same channel length h of 100 μm as an example (Movie S5, Supporting Information), the upper surface of the structured lithium metal anodes after 20 min lithium electroplating become smoother. And the length of the trunk of lithium dendrites in channels is shorten proportionally from 50 to 25 μm (Figs. S2d, S2e, and S2f, Supporting Information). While the final electroplated areal capacity at 10 min slightly increases from 10.5 to 11.8 mAh cm^{-2}, so does the total surface area which slightly increases from 47.3 to 51.0 cm^2 cm^{-2}. This indicates a similar convergent surface area per unit capacity S_c range from 4.2 to 4.5 cm^2 (mAh)$^{-1}$ at a prolonged electroplating (Fig. 5a and b). However, the current density varies different at the beginning stage and final stage of the lithium electroplating. With the channel width d decreases from 100 to 50 μm, the current density at 1 min increases from 90.0 to 161.4 mA cm^{-2}, while at 8 min it decreases from 46.8 to 19.5 mA cm^{-2} (Fig. 5a). Such difference in current density change is due to the different rate-determining step during the lithium electroplating process, which will be discussed later.

Supplementary data related to this article can be found at https://doi.org/10.1016/j.ensm.2019.03.029.

When the channel length h increases from 50 to 150 μm, taking the structure with the same channel width d of 66.7 μm for example (Movie S6, Supporting Information), the profile of every lithium dendrite in channels has no obvious difference (Figs. S2b, S2e, and S2h, Supporting Information). However, the final electroplated areal capacity at 10 min significantly increased from 6.9 to 15.6 mAh cm^{-2}. This is corresponding to the final deposit areal surface area of from 32.0 to 63.8 cm^2 cm^{-2} and a similar convergent S_c range from 4.1 to 4.6 cm^2 (mAh)$^{-1}$ at a prolonged electroplating (Fig. 5c and d). With the channel length h increases from 50 to 100 μm, the current density at 1 min increases from 70.4 to 160.1 mA cm^{-2}, and at 8 min it also increases from 22.2 to

38.4 mA cm^{-2}, which has a different change rule against that with different widths (Fig. 5c).

Supplementary data related to this article can be found at https://doi.org/10.1016/j.ensm.2019.03.029.

Why there is such different in current density change? We find that the current density change is highly depended on the rate-determining step at the beginning stage and final stage of the lithium electroplating. At the forepart of electroplating, there is enough space and lithium ion supplement in structure channels, the electroplating reaction rate is proportional to the electronic conductive surface area, which is accord with the structural areal surface area S_A. For instance, the S_A in Fig. 4d, e, and 4f increases from 3.0 to 5.0 cm^2 cm^{-2} (Table 1), along with the increase in current density with the decreased channel width d at $t = 1$ min. At the later electroplating process, the lithium dendrite growth fills in the narrow channels more quickly than the wide channels. When the channels are filled with electroplated lithium, the only growth direction is the upper direction, due to the channel block and ion barrier caused by grown lithium dendrites. Generally speaking, the later current density maintains higher if the 3D structure channel is with a higher ratio of pore volume to structural surface area, which is the reciprocal of S_V. For instance, the S_V in Fig. 4d, e, and 4f increases from 300.0 to 500.0 cm^2 cm^{-3} (Table 1), along with the decrease in current density with the decreased channel width d at $t = 8$ min, which mentioned before. As for the structures with different channel lengths, due to consistently larger current density with longer channel length at different times during electroplating (Fig. 5c), the final electroplated areal capacity can be significantly increased with the increase of channel length. Besides, the S_A increased from 2.5 to 5.5 cm^2 cm^{-2}, and S_V decreased from 500.0 to 366.7 cm^2 cm^{-3}, with h increasing from 50 to 150 μm (Fig. 4b, e, 4h, Table 1). This both guarantee a higher current density with longer channel length, consisting with the both increasement in current density at $t = 1$ min and 8 min with increasing channel length, which mentioned above. Thus, a small structural pore-volumetric surface area and a high areal pore volume afford enough space for lithium metal electroplating and lithium ion supplement, which guarantees a stable electrochemical performance with a high cycle capacity.

Furthermore, the surface area per unit capacity S_c of these structural lithium metal anodes in Fig. 4 are also converge to around 4.4 cm^2 (mAh)$^{-1}$ at a prolonged electroplating (Fig. 5b and d). Therefore, the quantity of SEI formation is also independent of the channel size of structured lithium metal anodes, only in direct proportion to the electroplated capacity.

To probe the role of S_A and S_V on lithium electroplating process in 3D structured lithium metal anodes, the scatter plot of different current densities at various electroplating times *versus* S_A and S_V are plotted as Fig. 5e and f, respectively. At the primary stage of lithium electroplating, the current density exhibits a remarkable linear correlation with S_A. The R-squared statistic of the linear fitting of $I = a \times S_A + b$ at the time before 4 min is all higher than 0.9, even equals to 0.9956 at 1 min (with $a = 37.03$, $b = -8.78$), while it is lower than 0.1 after 6 min (Fig. S3, Supporting Information). The electroplating reaction rate in the forepart kinetic process is limited by electron transfer in the composite Li metal anode. Therefore, a remarkable linear correlation is observed at the beginning of electroplating process. With enough lithium ion supplement and space provided by free pores in 3D hosts, higher conductive surface area brings more electroplating nucleation sites, which leading to a linearly higher electroplating reaction rate. Consequently, a 3D electronic conductive structured lithium metal anode with large S_A can guarantee a high electroplating rate during potentiostatic charging process or a low overpotential during galvanostatic charging process before the lithium dendrite growing to complete cover the structural conductive surface area.

At the final stage of lithium electroplating, the current density exhibits an inversely proportional relationship with structural pore-volumetric surface area S_V. The R-squared statistic of the inverse proportional fitting of $I = a/S_V + b$ at the time after 7 min is all higher than

Table 1
The structural parameters of simulated structured lithium metal anodes.

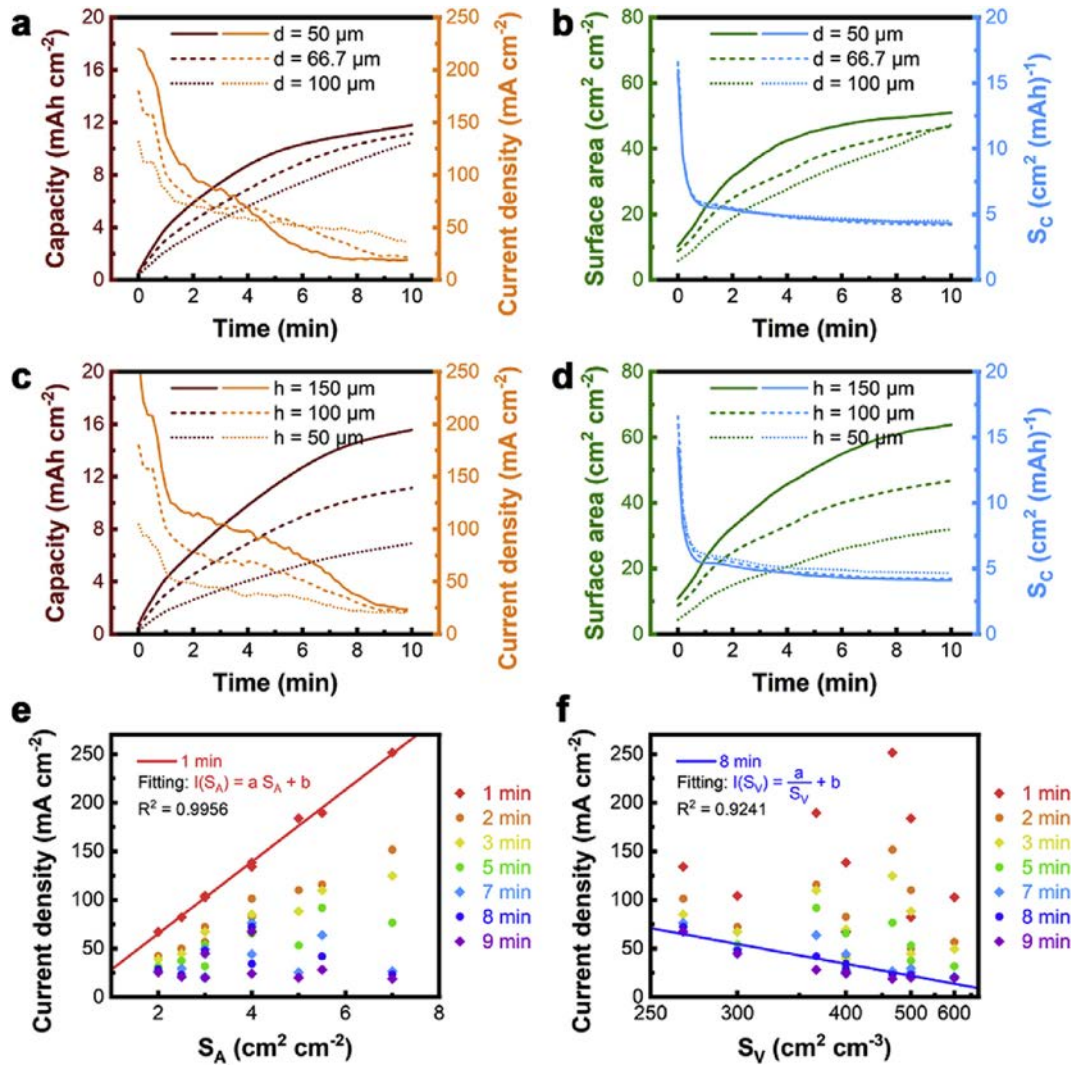| Figure	Channel width d [μm]	Channel length h [μm]	Structural areal surface area S_A [cm^2 cm^{-2}]	Structural pore-volumetric surface area S_V [cm^2 cm^{-3}]
4a	100.0	50.0	2.0	400.0
4b	66.7	50.0	2.5	500.0
4c	50.0	50.0	3.0	600.0
4d	100.0	100.0	3.0	300.0
4e	66.7	100.0	4.0	400.0
4f	50.0	100.0	5.0	500.0
4g	100.0	150.0	4.0	266.7
4h	66.7	150.0	5.5	366.7
4i	50.0	150.0	7.0	466.7

Fig. 5. Lithium dendrite growth influenced by the structural sizes. a,c) The electroplated capacity and current density curves, and b,d) the total surface area and surface area per capacity curves of the structured lithium metal anodes with a,b) different channel widths (the same channel length of $100\,\mu m$) or c,d) different channel lengths (the same channel width of $66.7\,\mu m$). e) The current density varies with structural areal surface area S_A for structured lithium metal anodes, showing a remarkable linear correlation at the primary stage of lithium electroplating. f) The current density varies with structural pore-volumetric surface area S_V (reciprocal coordinate) for structured lithium metal anodes, showing an inversely proportional relationship at the final stage of lithium electroplating.

0.8, which equals to 0.9241 at 8 min (with $a = 2.451 \times 10^4$, $b = -27.13$), while it is lower than 0.1 before 4 min (Fig. S3, Supporting Information). This inversely proportional relationship at the later stage of electroplating process is attributed to the regulation by ion transfer in electrolyte on electroplating reaction rate in later kinetic process. When the plated lithium fully covered the structural conductive surface area, and the lithium ion concentration in the pore center as well begins to decrease due to the continuous consumption of lithium ions, the reaction rate is then determined by the lithium ion transfer rate in electrolyte through these channels. With a higher ratio of pore volume to conductive surface area, there is more space for lithium to deposit and transfer from bulk electrolyte.

Under ideal condition, the current density at the ion transfer limited stage should be in direct proportion to the ratio of pore volume to conductive surface area, which is the reciprocal of structural pore-volumetric surface area S_V. However, the pore microstructures such as local surface curvatures, pore sectional sizes and shapes also impact the relationship between S_V and the current density. Consequently, the inverse proportional fitting is still with some irremovable error. In case of the inversely proportionally quadratic fitting of $I = a/S_V^2 + b/S_V + c$, the R-squared statistic at the time after 8 min can be all higher than 0.9, even

equals to 0.9931 at 9 min (with $a = 1.429 \times 10^7$, $b = -5.558 \times 10^4$, $c = 73.53$) (Figs. S3 and S4, Supporting Information). Therefore, a 3D electronic conductive structured lithium metal anode with a small S_V can guarantee a high electroplating rate during potentiostatic charging process or a low overpotential during galvanostatic charging process after the lithium deposit completely cover the structural conductive surface area at a high cycling capacity.

Such simulation results can initially guide the structural design and adjustment of 3D structured lithium metal anodes. For common structured electrodes fabricated by uniform frameworks, the structural areal surface area S_A and the structural pore-volumetric surface area S_V can be defined as

$$S_A = \text{SSA} \cdot \rho_f \cdot D = \text{SSA} \cdot D \cdot \rho_0 \cdot (1 - \varphi) \tag{1}$$

$$S_V = \text{SSA} \cdot \frac{\rho_f}{\varphi} = \text{SSA} \cdot \rho_0 \cdot \frac{1 - \varphi}{\varphi} \tag{2}$$

where SSA is the specific surface area of framework, ρ_f and ρ_0 is the apparent density of structured framework and the absolute density of framework material, respectively. φ is the porosity of structured frame-

work, and $\rho_f = \rho_0 \cdot (1 - \varphi)$ [40]. D is the thickness of the framework coated or assembled in structured electrodes. It should be noticed that with different frameworks, the SSA may also vary with D, ρ_0, and φ in different ways. Therefore, for specific framework materials or specific electrode preparation methods, specific optimizing strategies for higher S_A and smaller S_V are required. Based on Equations (1) and (2), it can be found that the ratio of S_A and S_V equals to the product of electrode thickness and porosity, which is indeed the areal pore volumes, i.e., $\frac{S_A}{S_V} = \varphi D$ (Fig. S5, Supporting Information). Consequently, for the same framework material, a higher areal pore volumes, a higher electrode porosity or a properly larger electrode thickness will be helpful to increase its high-rate performance. However, once the electrode thickness become very thick, the energy density of lithium metal batteries will be heavily reduced. Thus, the electrode thickness should be primarily decided based on the designed anode capacity.

The practicability of these models can be verified with various structured lithium metal anodes in literature. Guo and co-workers have described the impact of the pore sizes in 3D structured lithium metal anodes [32]. They employed a 3D Cu current collector with a structural areal surface area S_A of $45 \, \mathrm{cm}^2 \, \mathrm{cm}^{-2}$ and a structural pore-volumetric surface area S_V of $3 \times 10^4 \, \mathrm{cm}^2 \, \mathrm{cm}^{-3}$, which can theoretically support a maximum current density of $1658 \, \mathrm{mA} \, \mathrm{cm}^{-2}$ at the electron transfer controlled stage and a maximum typical current density of $71.7 \, \mathrm{mA} \, \mathrm{cm}^{-2}$ at the final ion transfer controlled stage at an constant overpotential of 0.10 V based on the fitting results of our phase field models. According to their experimental result, the 3D Cu current collector can cycle at $0.5 \, \mathrm{mA} \, \mathrm{cm}^{-2}$ with an overpotential around 0.02 V, and lithium can be plated inside the 3D Cu current collector at a high current density of $5 \, \mathrm{mA} \, \mathrm{cm}^{-2}$, which is consistent with the predictions of our model. Moreover, Chen and co-workers have employed carbon cloth to fabricate composite lithium metal anodes [27]. The carbon cloth is with a structural pore-volumetric surface area S_V of $1407 \, \mathrm{cm}^2 \, \mathrm{cm}^{-3}$, which can afford a high current density of $5 \, \mathrm{mA} \, \mathrm{cm}^{-2}$ in their experimental results. Such result is also consistent with the predict maximum current density in our model. Furthermore, consider the actual electrochemical reactions with the presence of SEI layer, the actual maximum current density at the electron transfer controlled stage should be much smaller than it in the models, while the actual maximum current density at the ion transfer controlled stage have little different with it in the models. It is worth noting that the exact quantitative relationship between current density, overpotential and structural parameters of 3D structured lithium metal anodes will change a lot with different electrolytes and SEI layers. Therefore, the special simulation is strong considered. In order to build a practical lithium metal battery with a very high energy density of more than $400 \, \mathrm{Wh} \, \mathrm{kg}^{-1}$, with an electrode loading more than $6 \, \mathrm{mAh} \, \mathrm{cm}^{-2}$, the 3D structured lithium metal anode need to be designed to meet specific rate and capacity requirements. Therefore, such a prediction model can effectively guide the design of structured lithium metal anodes.

To be sure, the phase filed model conducted here is still not perfect to describe the mechanisms in lithium electroplating process. But actually, numerical simulation methods have been paid increasing attention and made growing achievements in revealing the mechanisms in lithium metal anodes. Monroe and Newman leaded the theoretical investigation on the mechanisms of lithium dendrite nucleation and growth. The dendrite growth can considerably be slowed by reducing the current density [60–62]. Hoffmann and co-workers employed a coarse-grain Monte Carlo model to describe the ionic migration in time-dependent electric fields and were able to simulate the dendrite length during electroplating [63]. Guyer et al. pioneered a one-dimension phase field model to describe an electrochemical system, with a view to the equilibrium behavior and kinetic behavior for electroplating and electrostripping processes of a diffuse interface model in electrochemical system [56,57]. Then, Chen and co-workers employed a thermodynamically consistent phase-field model, accounting for the nonlinear reaction kinetics, to investigate the dendritic patterns during electrodeposition

processes [58,64,65]. Recently, Yan et al. integrated the nonlinear phase field lithium dendrite model and a heat transfer model to explore the thermal effect on the shape and size of lithium dendrites during the electroplating process [66]. Herein, we firstly employ the phase field model in 3D structured lithium metal anodes, and discover the relationship between electroplating reaction rate and the electrode structural parameters, indicating the conditions for electron transfer or ion transfer limited electroplating process. Beyond the design and adjustment of 3D structured lithium metal anodes, further numerical simulation is required in revealing the mechanism of lithium metal batteries.

Overall, we proposed a quantitative model to describe the Li metal anode with 3D interconnected hosts to deeply and rationally investigate the working mechanisms and plating/stripping processes of structured lithium metal anodes including the dendrite growth and dissolution process. Once a 3D host is applied in composite lithium metal anode, a small initial nucleation interval d_N can bring a uniform local deposit surface with small roughness. The branch of lithium dendrites can be shorten and even eliminated. Therefore, the growth of lithium dendrite branches is inhibited. A small channel width (pore size) d can bring a uniform plated surface of the whole electrode and shorten the trunk length of lithium dendrite, directly inhibiting the lithium dendrite growth. A longer channel length h can afford large pore volume for high cycling capacity. However, the influence of channel size is complicated. We found that the structural areal surface area S_A and the structural pore-volumetric surface area S_V have a directly impact on the electroplating behaviors. A large structural areal surface area S_A can linearly increase the electroplating rate at the beginning stage of electroplating, which is important for high rate cycles. Meanwhile, a small structural pore-volumetric surface area S_V can inversely increase the electroplating rate at the later stage of electroplating after lithium deposit completely covers the conductive surface and the reaction rate is limited by the lithium ion supply from electrolyte, which is essential for high capacity cycles. In addition, the quantity of SEI formation is proportionally to the increasing electroplated capacity, and have no significant relationship with the channel size nor the nucleation density in structured lithium metal anodes. Therefore, the best approach to decrease the SEI layer formation relies on the modification of surface energy of electroplated lithium, which can regulate the dendritic patterns and even into plane deposits, in other words, artificial protective/SEI layer is necessary, or the employment of solid state electrolyte.

3. Conclusions

The lithium dendrite growth is quantitatively described in various 3D conductive structured lithium metal anodes based on phase field models. With the proposed processing method to calculate deposit surface area of lithium dendrites and later quantitative analysis, the key determinants (including the structural areal surface area S_A and structural pore-volumetric surface area S_V) for lithium electroplating in 3D structured lithium metal anodes are proposed and identified. The S_A linearly determines the electroplating reaction rate in the forepart kinetic process, which is limited by electron transfer in the composite Li metal anode. In contrast, the S_V exhibits an inversely proportional relationship on the electroplating reaction rate in later kinetic process, which is limited by ion transfer in electrolyte in pore structures. Larger S_A and smaller S_V can both reduce the overpotential during galvanostatic cycles or increase the reaction rate during potentiostatic cycles for high rate and high capacity charge-discharge cycle processes in a working battery. The deposit surface area of lithium dendrites approaches proportionally to the increasing plated capacity. An ideal 3D structured lithium metal anode for high safety, high rate, high capacity, and high lifespan batteries requires (1) a small initial nucleation interval d_N, (2) a large structural areal surface area S_A, (3) a small structural pore-volumetric surface area S_V, and (4) a protective electrolyte-electrode interphase. With the quantitative simulation results and in-situ experimental observation, a better structured lithium metal anode can be designed to carry out the high-

energy-density lithium metal batteries with high charge-discharge rate and high cycling capacity.

4. Experimental section

4.1. In-situ observation of Li dendrite growth

A homemade optical cell with a quartz window was adopted for in situ observation. Two Li foil pressed on Cu current collector (4 mm × 8 mm) were employed as working electrode and counter electrode respectively. 1.0 M $LiPF_6$ in EC:DEC (v/v) = 1:1 (Beijing Institute of Chemical Reagents) was used as electrolyte. The cell was assembled and sealed in an Ar filled glove box with H_2O and O_2 contents <0.1 ppm. In-situ observation was realized under a metallurgical microscope and recorded by a charge coupled device camera (CCD). A Solartron 1470E electrochemical workstation (Solartron Analytical, UK) was employed for providing galvanostatic deposition. The test current densities were 2.0 or 5.0 mA cm^{-2}.

4.2. Phase field simulations

In the phase field models employed here, the electrochemical reaction can be illustrated as

$$Li^+ + e^- \rightarrow Li \tag{3}$$

The Gibbs free energy of this system can be expressed by

$$G = \int_V \left[f_{ch}(\boldsymbol{c}) + \frac{1}{2}\nabla\tilde{\boldsymbol{c}} \cdot \kappa\nabla\tilde{\boldsymbol{c}} + \rho_c\phi \right] dV \tag{4}$$

where $c = \{c, c_+, c_-\}$ is the set of concentrations of Li atom, Li^+ cation and PF_6^- anion, respectively. $f_{ch}(c)$ is the Helmholtz free energy density. $\frac{1}{2}\nabla c \cdot \kappa\nabla c$ is the gradient energy density, where κ is the anisotropic gradient coefficient, which associated with the surface energy. $\tilde{c}$ is the set of dimensionless concentrations as $\tilde{c} = \{\tilde{c} = c/c_s, \tilde{c}_+ = c_+/c_0, \tilde{c}_- = c_-/c_0\}$, where c_s is the site density of lithium metal and c_0 is the standard bulk concentration of electrolyte. $\rho_c\phi$ is the electrostatic energy density, in which ϕ is the electrostatic potential, and ρ_c is the charge density. V is the arbitrary volume.

The electrochemical reaction rate based on Butler-Volmer kinetics can be expressed by

$$R_e = -R_0\left\{\exp\left[\frac{(1-\alpha)nF\eta}{RT}\right] - \exp\left[\frac{-\alpha nF\eta}{RT}\right]\right\} \tag{5}$$

where R_0 is the exchange reaction rate. $1 - \alpha$ and α is the anodic and cathodic charge-transfer coefficients, respectively. n is the reaction electron number, which is 1 in the model. η is the overpotential. F, R, and T is the Faraday constant, molar gas constant, and temperature, respectively.

As a result of derivation, the partial differential equations describe the temporal evolution of phase field order parameter and Li^+ ion concentration is

$$\frac{\partial\xi}{\partial t} = -L_\sigma\left[g'(\xi) - \kappa\nabla^2\xi\right] - L_\eta h'(\xi)\left\{\exp\left[\frac{(1-\alpha)nF\eta_a}{RT}\right] - \tilde{c}_+\exp\left[\frac{-\alpha nF\eta_a}{RT}\right]\right\} \tag{6}$$

$$\frac{\partial\tilde{c}_+}{\partial t} = \nabla\cdot\left(D^{\text{eff}}\nabla\tilde{c}_+ + D^{\text{eff}}\frac{\tilde{c}_+nF}{RT}\nabla\phi\right) - \frac{c_s}{c_0}\frac{\partial\xi}{\partial t} \tag{7}$$

where L_σ is the interfacial mobility. L_η is the reaction constant. $g(\xi) = W\xi^2(1-\xi)^2$ is an arbitrary double well function to describe the two equilibrium states for electrode and electrolyte, where $W/16$ represents the barrier height. $h(\xi) = \xi^3(6\xi^2 - 15\xi + 10)$ is an interpolating function.

η_a is the activation overpotential. D^{eff} is the effective diffusion coefficient: $D^{\text{eff}} = D^e h(\xi) + D^s(1 - h(\xi))$, where D^e and D^s are the Li^+ diffusion coefficients in the electrode and the electrolyte, respectively.

The electrostatic potential based on Poisson equation can be expressed by

$$\nabla\cdot(\sigma^{\text{eff}}\nabla\phi) = I_R = nFc_s\frac{\partial\xi}{\partial t} \tag{8}$$

where σ^{eff} is the effective conductivity: $\sigma^{\text{eff}} = \sigma^e h(\xi) + \sigma^s(1 - h(\xi))$, where σ^e and σ^s are the conductivities in the electrode and the electrolyte, respectively.

The parameters mentioned above are detailed in Table S1. This phase field model is simulated by finite element method on COMSOL Multiphysics 5.4. The size of the simulated model is 100 μm × 100 μm for plane surface with single nucleation site, and 200 μm × 200 μm for plane surface with multiple nucleation sites and all structured lithium metal anodes, for the model with single nucleation site can take up less space for better resolution. The maximum grid spacing is 0.75 μm. Dirichlet boundary conditions are applied to solve the equations from Eqs. (4)–(6). The overpotential between electrolyte and electrode is set as 0.10 V. The deposit areal surface area can be calculated by solving the numerical length of the contour line at $\xi = 0.5$. Besides, the electroplated areal capacity can be calculated by integrating ξ in the whole simulation area. The current density during simulated potentiostatic electroplating is calculated by the forward difference method based on the electroplated areal capacity.

Appendix A. Supplementary data

Supplementary data to this article can be found online at https://doi.org/10.1016/j.ensm.2019.03.029.

References

[1] X.-B. Cheng, R. Zhang, C.-Z. Zhao, Q. Zhang, Chem. Rev. 117 (2017) 10403–10473.
[2] M. Armand, J.M. Tarascon, Nature 451 (2008) 652–657.
[3] J.M. Tarascon, M. Armand, Nature 414 (2001) 359–367.
[4] Y. Li, Y. Li, A. Pei, K. Yan, Y. Sun, C.-L. Wu, L.-M. Joubert, R. Chin, A.L. Koh, Y. Yu, J. Perrino, B. Butz, S. Chu, Y. Cui, Science 358 (2017) 506–510.
[5] B. Liu, J.-G. Zhang, W. Xu, Joule 2 (2018) 833–845.
[6] W. Xu, J.L. Wang, F. Ding, X.L. Chen, E. Nasybutin, Y.H. Zhang, J.G. Zhang, Energy Environ. Sci. 7 (2014) 513–537.
[7] X.-B. Cheng, R. Zhang, C.-Z. Zhao, F. Wei, J.-G. Zhang, Q. Zhang, Adv. Sci. 3 (2016) 1500213.
[8] X.-B. Cheng, C. Yan, J.-Q. Huang, P. Li, L. Zhu, L. Zhao, Y. Zhang, W. Zhu, S.-T. Yang, Q. Zhang, Energy Storage Mater. 6 (2017) 18–25.
[9] L. Wang, Z. Zhou, X. Yan, F. Hou, L. Wen, W. Luo, J. Liang, S.X. Dou, Energy Storage Mater. 14 (2018) 22–48.
[10] X. Liang, Q. Pang, I.R. Kochetkov, M.S. Sempere, H. Huang, X. Sun, L.F. Nazar, Nat. Energy 2 (2017) 17119.
[11] Y. Liu, D. Lin, Y. Li, G. Chen, A. Pei, O. Nix, Y. Li, Y. Cui, Nat. Commun. 9 (2018) 3656.
[12] X. Fan, L. Chen, X. Ji, T. Deng, S. Hou, J. Chen, J. Zheng, F. Wang, J. Jiang, K. Xu, C. Wang, Chemistry 4 (2018) 174–185.
[13] L. Wang, L. Zhang, Q. Wang, W. Li, B. Wu, W. Jia, Y. Wang, J. Li, H. Li, Energy Storage Mater. 10 (2018) 16–23.
[14] C. Yan, X.-B. Cheng, Y. Tian, X. Chen, X.-Q. Zhang, W.-J. Li, J.-Q. Huang, Q. Zhang, Adv. Mater. 30 (2018) 1707629.
[15] R. Xu, X.Q. Zhang, X.B. Cheng, H.J. Peng, C.Z. Zhao, C. Yan, J.Q. Huang, Adv. Funct. Mater. 28 (2018) 1705838.
[16] Y. Liu, D. Lin, P.Y. Yuen, K. Liu, J. Xie, R.H. Dauskardt, Y. Cui, Adv. Mater. 29 (2017) 1605531.
[17] X.-Q. Zhang, X. Chen, R. Xu, X.-B. Cheng, H.-J. Peng, R. Zhang, J.-Q. Huang, Q. Zhang, Angew. Chem. Int. Ed. 56 (2017) 14207–14211.

[18] C. Yang, L. Zhang, B. Liu, S. Xu, T. Hamann, D. McOwen, J. Dai, W. Luo, Y. Gong, E.D. Wachsman, L. Hu, Proc. Natl. Acad. Sci. U.S.A. 115 (2018) 3770–3775.

[19] C.-Z. Zhao, P.-Y. Chen, R. Zhang, X. Chen, B.-Q. Li, X.-Q. Zhang, X.-B. Cheng, Q. Zhang, Sci. Adv. 4 (2018) eaat3446.

[20] C.-Z. Zhao, X.-Q. Zhang, X.-B. Cheng, R. Zhang, R. Xu, P.-Y. Chen, H.-J. Peng, J.-Q. Huang, Q. Zhang, Proc. Natl. Acad. Sci. U.S.A. 114 (2017) 11069–11074.

[21] D. Zhou, R. Liu, Y.-B. He, F. Li, M. Liu, B. Li, Q.-H. Yang, Q. Cai, F. Kang, Adv. Energy Mater. 6 (2016) 1502214.

[22] R. Zhang, N.-W. Li, X.-B. Cheng, Y.-X. Yin, Q. Zhang, Y.-G. Guo, Adv. Sci. 4 (2017) 1600445.

[23] D. Lin, Y. Liu, Z. Liang, H.-W. Lee, J. Sun, H. Wang, K. Yan, J. Xie, Y. Cui, Nat. Nanotechnol. 11 (2016) 626–632.

[24] G.Y. Zheng, S.W. Lee, Z. Liang, H.W. Lee, K. Yan, H.B. Yao, H.T. Wang, W.Y. Li, S. Chu, Y. Cui, Nat. Nanotechnol. 9 (2014) 618–623.

[25] A. Wang, S. Tang, D. Kong, S. Liu, K. Chiou, L. Zhi, J. Huang, Y.-Y. Xia, J. Luo, Adv. Mater. 30 (2018) 1703891.

[26] F. Guo, Y. Wang, T. Kang, C. Liu, Y. Shen, W. Lu, X. Wu, L. Chen, Energy Storage Mater. 15 (2018) 116–123.

[27] Y. Zhou, Y. Han, H. Zhang, D. Sui, Z. Sun, P. Xiao, X. Wang, Y. Ma, Y. Chen, Energy Storage Mater. 14 (2018) 222–229.

[28] K. Yan, B. Sun, P. Munroe, G. Wang, Energy Storage Mater. 11 (2018) 127–133.

[29] Z. Sun, S. Jin, H. Jin, Z. Du, Y. Zhu, A. Cao, H. Ji, L.-J. Wan, Adv. Mater. 30 (2018) 1800884.

[30] L. Fan, S. Li, L. Liu, W. Zhang, L. Gao, Y. Fu, F. Chen, J. Li, H.L. Zhuang, Y. Lu, Adv. Energy Mater. 8 (2018) 1802350.

[31] R. Zhang, X.-B. Cheng, C.-Z. Zhao, H.-J. Peng, J.-L. Shi, J.-Q. Huang, J. Wang, F. Wei, Q. Zhang, Adv. Mater. 28 (2016) 2155–2162.

[32] C.P. Yang, Y.X. Yin, S.F. Zhang, N.W. Li, Y.G. Guo, Nat. Commun. 6 (2015) 8058.

[33] J. Lang, Y. Jin, X. Luo, Z. Liu, J. Song, Y. Long, L. Qi, M. Fang, Z. Li, H. Wu, J. Mater. Chem. A 5 (2017) 19168–19174.

[34] S. Liu, X. Xia, Y. Zhong, S. Deng, Z. Yao, L. Zhang, X.-B. Cheng, X. Wang, Q. Zhang, J. Tu, Adv. Energy Mater. 8 (2018) 1702322.

[35] H. Zhao, D. Lei, Y.-B. He, Y. Yuan, Q. Yun, B. Ni, W. Lv, B. Li, Q.-H. Yang, F. Kang, J. Lu, Adv. Energy Mater. 8 (2018) 1800266.

[36] S.-H. Wang, Y.-X. Yin, T.-T. Zuo, W. Dong, J.-Y. Li, J.-L. Shi, C.-H. Zhang, N.-W. Li, C.-J. Li, Y.-G. Guo, Adv. Mater. 29 (2017) 1703729.

[37] X. Zhang, R. Lv, A. Wang, W. Guo, X. Liu, J. Luo, Angew. Chem. Int. Ed. 57 (2018) 15028–15033.

[38] X.-B. Cheng, H.-J. Peng, J.-Q. Huang, R. Zhang, C.-Z. Zhao, Q. Zhang, ACS Nano 9 (2015) 6373–6382.

[39] F. Shen, F. Zhang, Y. Zheng, Z. Fan, Z. Li, Z. Sun, Y. Xuan, B. Zhao, Z. Lin, X. Gui, X. Han, Y. Cheng, C. Niu, Energy Storage Mater. 13 (2018) 323–328.

[40] R. Zhang, X. Chen, X. Shen, X.-Q. Zhang, X.-R. Chen, X.-B. Cheng, C. Yan, C.-Z. Zhao, Q. Zhang, Joule 2 (2018) 764–777.

[41] L. Liu, Y.-X. Yin, J.-Y. Li, S.-H. Wang, Y.-G. Guo, L.-J. Wan, Adv. Mater. 30 (2018) 1706216.

[42] T.-T. Zuo, Y.-X. Yin, S.-H. Wang, P.-F. Wang, X. Yang, J. Liu, C.-P. Yang, Y.-G. Guo, Nano Lett. 18 (2018) 297–301.

[43] R. Zhang, X.-R. Chen, X. Chen, X.-B. Cheng, X.-Q. Zhang, C. Yan, Q. Zhang, Angew. Chem. Int. Ed. 56 (2017) 7764–7768.

[44] C. Yang, Y. Yao, S. He, H. Xie, E. Hitz, L. Hu, Adv. Mater. 29 (2017) 1702714.

[45] S. Liu, X. Xia, Z. Yao, J. Wu, L. Zhang, S. Deng, C. Zhou, S. Shen, X. Wang, J. Tu, Small Methods 2 (2018) 1800035.

[46] P. Xue, S. Liu, X. Shi, C. Sun, C. Lai, Y. Zhou, D. Sui, Y. Chen, J. Liang, Adv. Mater. 30 (2018) 1804165.

[47] C. Jin, O. Sheng, J. Luo, H. Yuan, C. Fang, W. Zhang, H. Huang, Y. Gan, Y. Xia, C. Liang, J. Zhang, X. Tao, Nano Energy 37 (2017) 177–186.

[48] W. Deng, W. Zhu, X. Zhou, Z. Liu, Energy Storage Mater. 15 (2018) 266–273.

[49] H. Zhang, X. Liao, Y. Guan, Y. Xiang, M. Li, W. Zhang, X. Zhu, H. Ming, L. Lu, J. Qiu, Y. Huang, G. Cao, Y. Yang, L. Mai, Y. Zhao, H. Zhang, Nat. Commun. 9 (2018) 3729.

[50] Y. Zhang, W. Luo, C. Wang, Y. Li, C. Chen, J. Song, J. Dai, E.M. Hitz, S. Xu, C. Yang, Y. Wang, L. Hu, Proc. Natl. Acad. Sci. U.S.A. 114 (2017) 3584–3589.

[51] W. Liu, D. Lin, A. Pei, Y. Cui, J. Am. Chem. Soc. 138 (2016) 15443–15450.

[52] J. Xie, J. Wang, H.R. Lee, K. Yan, Y. Li, F. Shi, W. Huang, A. Pei, G. Chen, R. Subbaraman, J. Christensen, Y. Cui, Sci. Adv. 4 (2018) eaat5168.

[53] D. Lin, Y. Liu, Y. Li, Y. Li, A. Pei, J. Xie, W. Huang, Y. Cui, Nat. Chem. 11 (2019) 382–389.

[54] H. Kim, D.A. Boysen, J.M. Newhouse, B.L. Spatocco, B. Chung, P.J. Burke, D.J. Bradwell, K. Jiang, A.A. Tomaszowska, K. Wang, W. Wei, L.A. Ortiz, S.A. Barriga, S.M. Poizeau, D.R. Sadoway, Chem. Rev. 113 (2013) 2075–2099.

[55] M. Winter, B. Barnett, K. Xu, Chem. Rev. 118 (2018) 11433–11456.

[56] J.E. Guyer, W.J. Boettinger, J.A. Warren, G.B. McFadden, Phys. Rev. E 69 (2004) 021604.

[57] J.E. Guyer, W.J. Boettinger, J.A. Warren, G.B. McFadden, Phys. Rev. E 69 (2004) 021603.

[58] L. Chen, H.W. Zhang, L.Y. Liang, Z. Liu, Y. Qi, P. Lu, J. Chen, L.-Q. Chen, J. Power Sources 300 (2015) 376–385.

[59] A. Pei, G. Zheng, F. Shi, Y. Li, Y. Cui, Nano Lett. 17 (2017) 1132–1139.

[60] C. Monroe, J. Newman, J. Electrochem. Soc. 151 (2004) A880–A886.

[61] C. Monroe, J. Newman, J. Electrochem. Soc. 152 (2005) A396–A404.

[62] C. Monroe, J. Newman, J. Electrochem. Soc. 150 (2003) A1377–A1384.

[63] A. Aryanfar, D. Brooks, B.V. Merinov, W.A. Goddard, A.J. Colussi, M.R. Hoffmann, J. Phys. Chem. Lett. 5 (2014) 1721–1726.

[64] H.-W. Zhang, Z. Liu, L. Liang, L. Chen, Y. Qi, S.J. Harris, P. Lu, L.-Q. Chen, ECS Trans. 61 (2014) 1–9.

[65] L. Liang, Y. Qi, F. Xue, S. Bhattacharya, S.J. Harris, L.-Q. Chen, Phys. Rev. E 86 (2012) 051609.

[66] H.H. Yan, Y.H. Bie, X.Y. Cui, G.P. Xiong, L. Chen, Energy Convers. Manag. 161 (2018) 193–204.